



ORIGINAL PAPER

MODELLING THE SENSITIVITY OF UNDERGROUND SPACE STABILITY TO THE *IN SITU* STRESS UNCERTAINTIES: CASE STUDY AT THE BUKOV UNDERGROUND RESEARCH FACILITY PHASE II (ROŽNÁ MINE, CZECHIA)

Libin GONG (巩利斌)^{1, 2)}*, Kamil SOUCEK¹⁾, Petr WACLAWIK¹⁾, Martin VAVRO¹⁾,
Lubomir STAS¹⁾, Jan NEMCIK²⁾ and Sahendra RAM³⁾

¹⁾ Department of Geomechanics and Mining Research, Institute of Geonics of the Czech Academy of Sciences, Ostrava, 70800, Czechia

²⁾ School of Civil, Mining and Environmental Engineering, Faculty of Engineering and Information Sciences, University of Wollongong, Wollongong, 2500, Australia

³⁾ Department of Mining Engineering, National Institute of Technology, Rourkela, Odisha, India

*Corresponding author's e-mail: libin.gong@ugn.cas.cz

ARTICLE INFO	ABSTRACT
Article history: Received 29 March 2021 Accepted 31 May 2021 Available online 16 June 2021	
Keywords: Numerical modelling <i>in situ</i> stress Strength-stress ratio Roadway convergence Stability model	Numerical modelling has been widely used in the underground excavation design, where the <i>in situ</i> stress state plays a crucial role in the stability analysis. However, determination of an exact stress state for a specific geological region remains uncertain due to the complicated tectonic nature and measurement limitations. The stability is thus better analysed by considering the <i>in situ</i> stress as a finite spectrum and pinpointing the possible worst-case scenario. The most probable scenarios of <i>in situ</i> stress states in the Rožná mine area were analysed based on the varying trends in principal stress ratio and mean stress values obtained from four different measurement/analysis campaigns. The influence of different <i>in situ</i> stress judgement on the deformation and failure characteristics of the Bukov Underground Research Facility (URF) (Phase II, Czech) were investigated by the finite volume program FLAC3D. Results show that the increased horizontal stress anisotropy and the mean stress level jointly increase the overall deformation and lower the URF stability. Such influences on the roadway horizontal convergence are more considerable than the vertical ones. A mathematical model considering mean stress and horizontal stress ratio was proposed to quantitatively describe the overall stability, especially useful for excavations possessing complicated configuration.

1. INTRODUCTION

Deep geological repositories (DGRs) have been constructed all over the world for disposal of high-level radioactive waste and spent nuclear fuel, which has been widely accepted to be the safest way of long-term isolation and containment of such waste materials (Apted and Ahn, 2017; Feiveson et al., 2011). A large number of underground research facilities (URFs) have also been built in many countries to investigate the geological, geomechanical and environmental issues of such DGRs and to study their isolation ability and performance (Apted, 2019; Bukovská et al., 2019; Delay et al., 2014; Laverov et al., 2016; NEA-OECD, 2013; Wang et al., 2018). The first part of the Bukov URF, which contains 475 m of galleries in total, was successfully constructed between 2013 and 2017 in the Rožná Mine area (hereinafter referred to as the Bukov URF – Phase I) (Souček et al., 2017). Recently, it is planned to expand the existing capacity of URF by excavating new galleries (hereinafter referred to as the Bukov URF – Phase II) with a total length of 860 m in geotechnical conditions.

The Bukov URF – Phase II is designed to be located at a depth of 550 m below ground level in

crystalline complexes of the Bohemian Massif. The stated depth is the same as already existing Bukov URF – Phase I and corresponds with the proposed disposal depth of the final locality for the national DGR. Five groups of laboratory roadways/chambers and two ventilation channels are to be excavated along a main transport roadway maintained from the original uranium mining area. Before the construction commencement of the Bukov URF – Phase II, it is essential to evaluate the feasibility and stability of the designed roadway and chamber layouts. The complex 3-dimensional (3D) geometry configuration of the caverns, *in situ* stress states and the existence of foliation in the metamorphic rock mass are all important parameters dominating the URF stability. Due to such characteristics of complexity, stability analysis or the estimation of the factor of safety (FoS) for the cavern groups is better to be conducted through numerical simulation (Peng et al., 2019).

When numerically analysing the excavation stability, the *in situ* stress state is one of the most important parameters dominating the FoS (Barton et al., 1974; Brady and Brown, 2007; Singh and Goel, 2011). The regional *in situ* stress should be determined by combining and integrating existing available

geological data, field stress measurement results and numerical modelling (Stephansson and Zang, 2012). So far, all kinds of methods have been established to measure the *in situ* stress, including hydraulic fracturing, hydraulic tests on pre-existing fractures, sleeve fracturing, borehole relief, and borehole breakout etc. (Amadei and Stephansson, 1997; Haimson and Cornet, 2003; Hudson et al., 2003; Sjöberg et al., 2003; Zang and Stephansson, 2010). However, the inaccuracy and imprecision during *in situ* stress measurement is inevitable (Sjöberg et al., 2003). Even though large numbers of *in situ* measurement have been conducted, the results could still lie within a certain range. Complicated crustal movement and structure formation in the history make the engineering judgement for one exact *in situ* stress state in the region even more difficult and impractical. How to determine the input values of the far-field stresses for the related numerical model is a considerable question yet barely considered during engineering consultancy and assessment. Different combinations of three principal stress components in the model may lead to significantly different results (Saeidi et al., 2021). The worst-case scenario should be identified to avoid overestimation of the safety factor of the excavation. Hence, sensibility analysis using the upper and lower limits of the field-measured *in situ* stress data is necessary.

This paper investigated the influence of different *in situ* stress states on the stability of a planned Bukov URF – Phase II located 550 m deep underground in the Czech Republic, within the scope of real measurement data obtained from different locations in the excavation region. The Itasca program Fast Lagrangian Analysis of Continua in 3 Dimensions (FLAC3D) (Itasca Consulting Group, 2012) is employed in this paper to analyse the stability of the URF, which has been widely adopted to numerically model and analyse the stability of engineering projects ranging from underground excavations to rock slopes on the ground surface (Corkum et al., 2018; Napa-García et al., 2019; Renani and Martin, 2020). The results highlighted the significance and necessity of careful treatment of the field-measured *in situ* stress values for the application in numerical modelling, and proposed novel methods to quantitatively describe the overall stability of similar underground excavations with complicated configuration.

2. GEOLOGICAL BACKGROUND

2.1. LITHOLOGY

The region of interest is formed by a highly metamorphosed volcano-sedimentary rock sequence at the north-eastern edge of the Strážek Moldanubicum Unit of the Bohemian Massif (Bukovská et al., 2019; Kříbek and Hájek, 2005; Ptáček et al., 2013; Souček et al., 2017; Vavro et al., 2015). The dominant rock types are paragneisses, migmatites and amphibolites with minor intercalation of calc-silicate rocks, marbles, granulites, granites/pegmatites, and peridotites. Both basic

lithologies, i.e. original metapelites (paragneisses) and metabasites (amphibolites) are affected by different degree of migmatization and are usually connected by gradual mutual transitions. The subjected area of Bukov URF – Phase II is formed mainly (in about 90 % of the area) by: (1) medium- to coarse-grained migmatites, and (2) fine- to medium-grained, slightly- to medium-migmatized biotite- to biotite-amphibole paragneisses with transition to biotite amphibolites (Fig. 2.1). These two lithology types are very close to each other in terms of geomechanical properties. For simplicity, we consider the rock masses in this region as quasi-homogeneous and consist of one general rock type with similar mechanical properties.

2.2. GEOLOGICAL STRUCTURES

As shown in Figure 2.1, the whole rock sequence in the area of interest is trending relatively monotonously in the directions NW–SE to NNW–SSE. The dominant system of metamorphic fabric is represented by metamorphic foliations, in general gently to moderately dipping towards SW.

The first-order tectonic structure (zone R–1) occurs in the immediate vicinity of the survey area. This fault zone has a direction of N–S to NNW–SSE and a general dip of 45–55° to W, representing a cataclastic to mylonitized zone with a thickness of about 5–15 m and a strike length of up to 15 km (Kříbek and Hájek, 2005). In terms of mineralization, zone R–1 is one of the two main ore-bearing structures of the Rožná uranium deposit. The second-order tectonic structures (e.g. zone R–17) are spatially and probably also genetically associated with zone R–1.

2.3. EVALUATION OF GEOMECHANICAL PROPERTIES OF ROCK MASSES

The input mechanical and deformation properties of the Bukov URF – Phase II rock mass, needed for the numerical model, were determined based on available geological survey and laboratory testing data. More specifically, three types of rocks tested within previous projects (Bukovská et al., 2020; Souček et al., 2018) which are petrographically very similar to Bukov URF – Phase II rocks (Fig. 2.1) were chosen. Laboratory testing was conducted in three different directions to their metamorphic foliation planes. The aim was to capture the anisotropy of mechanical and deformation properties, which is in the rock mass in question very well-known (Bukovská et al., 2020; Bukovská et al., 2019; Souček et al., 2018; Vavro et al., 2015). Testing results are summarised in Table 2.1.

The ubiquitous joint model is an appropriate failure criterion for the rock mass with clear anisotropy, considering the role of weak planes of specific orientation. However, it is difficult to determine the material properties compared with the Hoek-Brown criterion where systematic guidelines for the properties assignment have been established. As the ubiquitous joint model does not consider the

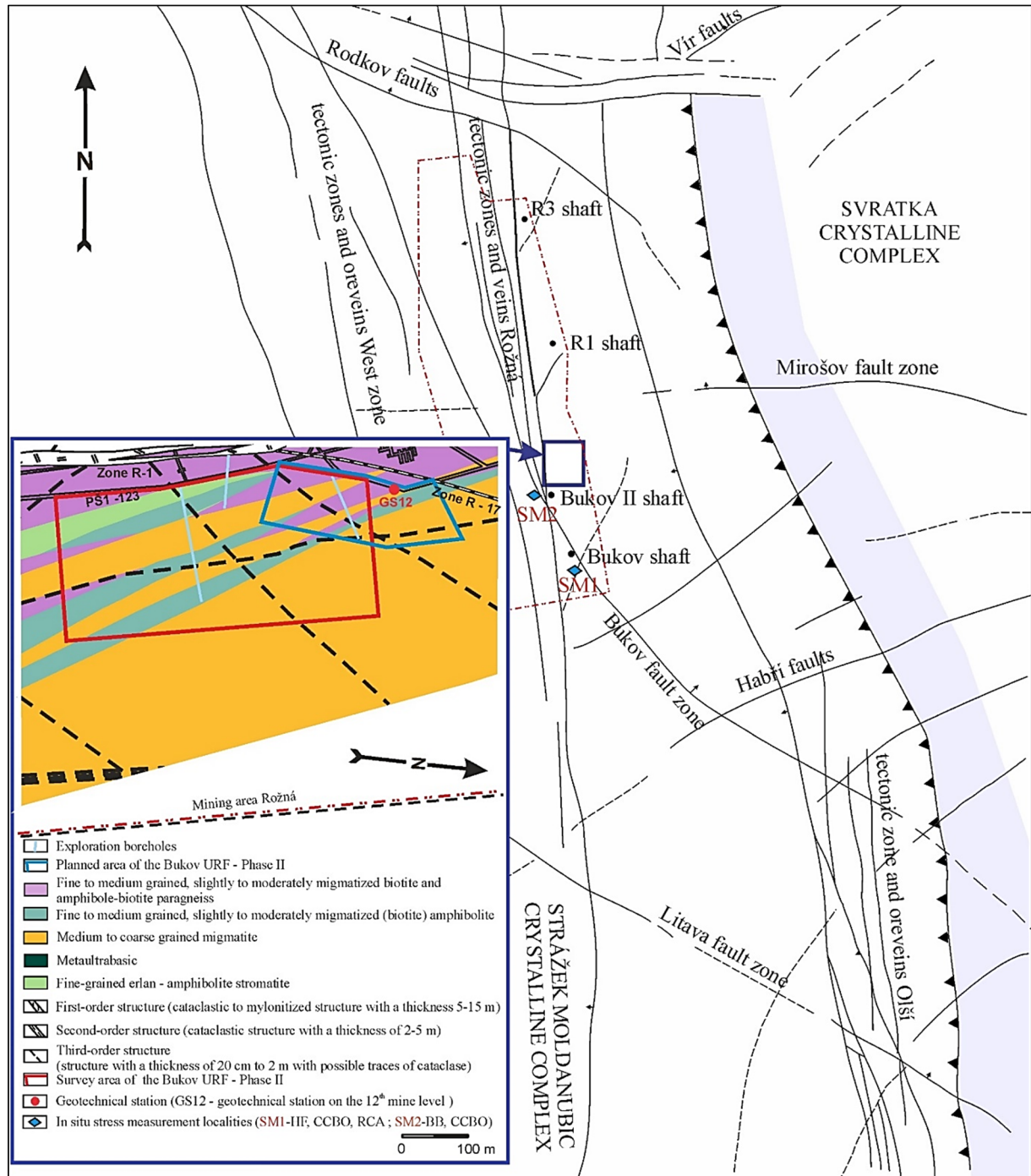


Fig. 2.1 Main fault structures and geological condition in the area of interest (Patocka and Jaros, 2020; Ptáček et al., 2013).

effects of joint spacing, length and stiffness, as well as the scale effect, complicated calibration is needed to select the appropriate model properties (Sainsbury and Sainsbury, 2017). Despite some limitations of the Hoek-Brown criterion e.g. the ignorance of the intermediate principal stress and rock anisotropy, it has been applied in many projects around the world and has been found to provide satisfactory estimates (Hoek and Brown, 2019). Hence, the Hoek-Brown model was adopted in this paper.

Based on the testing results, the Hoek-Brown failure envelope was determined for these samples using *RocData* toolkit (Rocscience Inc., 2017). The Hoek-Brown parameters for three different loading directions were then averaged to obtain the general failure envelopes for the quasi-homogeneous lithological unit. An example is illustrated in Figure 2.2.

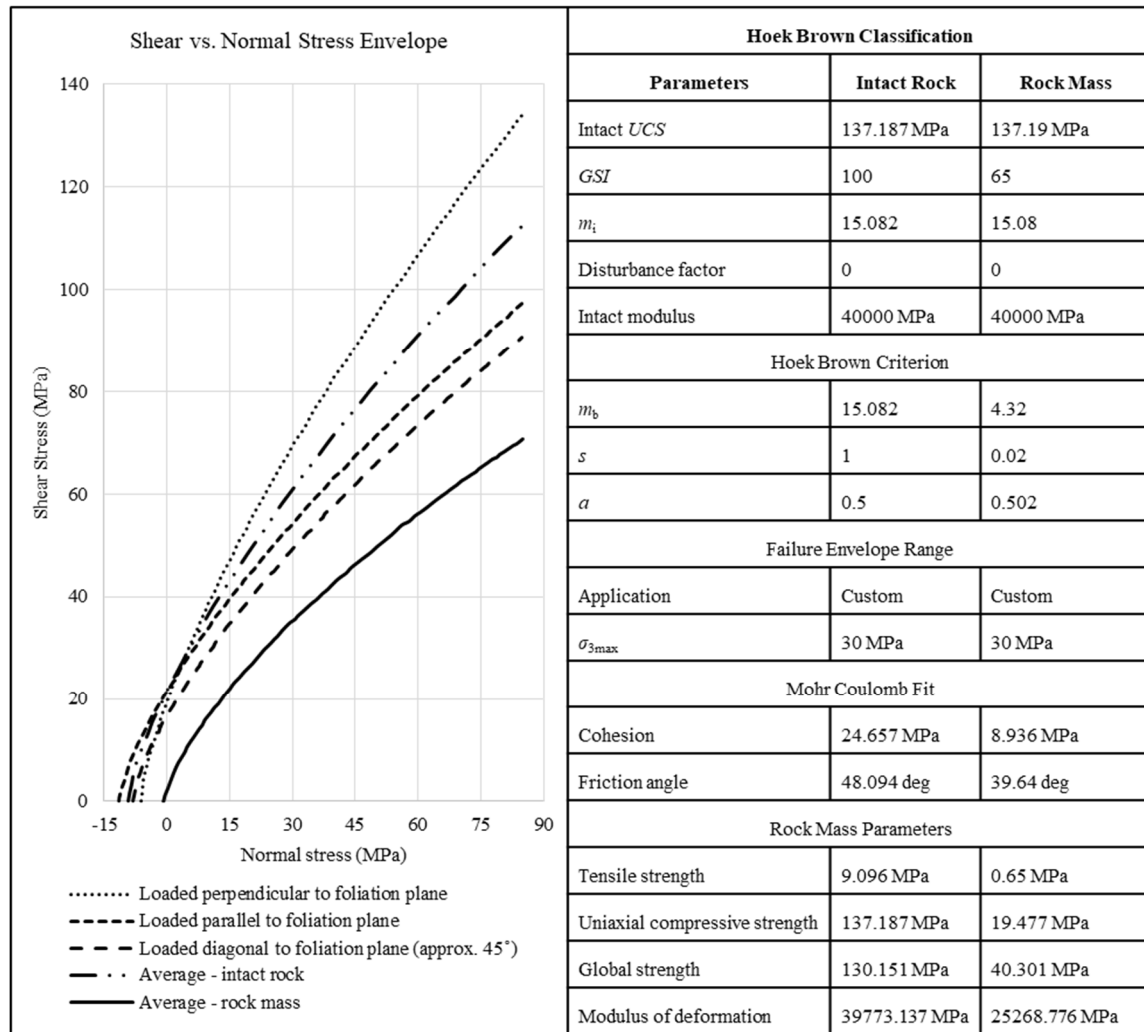


Fig. 2.2 Example for generating the average Hoek-Brown failure envelopes (sample V22).

Table 2.1 Average values of physical-mechanical properties of selected intact rocks from Rožná mine area (Bukovská et al., 2020; Souček et al., 2018).

Property	Unit	sample T3	sample V22-R3	sample V22
Lithology	–	Biotite-amphibole gneiss	Biotite migmatite	Sillimanite-biotite migmatite
Bulk density, ρ	kg/m ³	2836	2742	2635
UCS, σ_{ci} – direction K	MPa	165	165	160
UCS, σ_{ci} –direction P	MPa	195	126	111
UCS, σ_{ci} – direction S	MPa	147	74	82
Young's modulus, E_i (K)	GPa	45	41	41
Young's modulus, E_i (P)	GPa	56	54	44
Young's modulus, E_i (S)	GPa	49	29	32
Poisson ratio, ν (K)	–	0.15	0.17	0.19
Poisson ratio, ν (P)	–	0.17	0.16	0.17
Poisson ratio, ν (S)	–	0.14	0.12	0.1
Splitting tensile strength, σ_{ti} (K)	MPa	12.0	7.8	6.2
Splitting tensile strength, σ_{ti} (P)	MPa	12.8	12.7	11.1
Splitting tensile strength, σ_{ti} (S)	MPa	10.9	10.4	8.1

Note: UCS – uniaxial compressive strength; K – direction of loading perpendicular to foliation plane; P – direction of loading parallel to foliation plane; S – direction of loading diagonal (approximately 45°) to metamorphic foliation plane; sample T3 – level 12, Bukov URF – Phase I, access gallery BZ-XIIJ; sample V22-R3 – level 22, R3 shaft; sample V22 – level 22, R7S shaft.

To extrapolate the averaged Hoek-Brown parameters from intact rock samples to filed-scale values, the Geological Strength Index (*GSI*) of the rock mass was employed (Hoek et al., 2013). Structural characteristics including persistence, roughness, undulation, and opening and filling of rock mass discontinuities were previously documented on the uncovered opening walls within the Bukov URF – Phase I (Bukovská et al., 2019; Souček et al., 2018). The *GSI* was then calculated using two different methods:

$$GSI = 1.5JCond_{89} + RQD / 2 \quad (2.1)$$

and

$$GSI = 52J_r/(J_a + J_r) + RQD/2 \quad (2.2)$$

where, *RQD* is Rock Quality Designation index value, *JCond*₈₉ is Joint Condition rating according to Bieniawski (1989) and the joint roughness number *J_r* and joint alteration number *J_a* are parameters in the *Q*-system (Barton et al., 1974).

The estimated *RQD* value for the rock mass of the whole Rožná uranium mine area is mostly between 60–65 %, peak up to 70 to 80 % (Bukovská et al., 2020; Bukovská et al., 2019; Souček et al., 2018; Souček et al., 2017; Vavro et al., 2015). However, Patocka and Jaros (2020) state an average *RQD* value of up to about 86 % in the area of interest. We have chosen the *RQD* value of 60 % for the calculation of *GSI* out of concern for safety. The values of other parameters (*JCond*₈₉, *J_r* and *J_a*) were determined from a distribution analysis of the discontinuity factors (e.g. persistence, roughness, etc.) expressed by a weighted average. Table 2.2 shows the determined geological input values for the calculation of *GSI* under the most probable occurrences of *RQD* values at Bukov URF – Phase II. It is clear that at the condition of *RQD* = 60 %, *GSI* varies in the range of 63–67. Hence, a value of 65 was chosen for estimating the filed-scale geomechanical properties of the above-mentioned intact rock samples. The obtained Hoek-Brown parameters for the rock mass were further averaged to describe the quasi-homogeneous rock mass for the numerical modelling. In this way, both the anisotropic rock fabric (foliation) and the

geological structure are taken into account. The failure envelope representing the macro-scale rock mass properties corresponding to the sample V22 (see Table 2.1) was also shown in Figure 2.2.

Final input properties for the Hoek-Brown model are summarised in Table 2.3.

2.4. STRESS STATE OF ROCK MASSES

One of the typical features of the rock mass at the Bukov region is relatively significant anisotropy, verified both physically (e.g. ultrasonic wave velocity, thermal conductivity and specific heat capacity) and mechanically (e.g. splitting tensile strength and uniaxial compressive strength) (Bukovská et al., 2020; Bukovská et al., 2019; Souček et al., 2018; Vavro et al., 2015). The high degree of textural anisotropy of rocks, as well as the relatively significant disturbance of the rock mass by ductile and brittle tectonics, result in the *in situ* stress field of the rock mass in this region as highly anisotropic.

Over the years abundant *in situ* stress measurements have been conducted in the Rožná mine region, with the measurement depth ranging from 520 m to 1183 m, as summarised in Table 2.4 (Bukovská et al., 2020; Souček et al., 2018). Although four different methods have been used for better reliability, i.e. borehole breakout (BB), hydraulic fracturing (HF), compact conical ended borehole overcoring (CCBO), and roadway convergence analysis (RCA), considerable scatter is still observed. Taking into account that a “stress decoupling” effect may exist causing significant difference in stresses at shallow depth and at great depth (Stephansson and Zang, 2012), and the fact that Bukov URF – Phase II is located at a depth of around 550 m, the stress data obtained at 500–600 m depth were selected for the *in situ* stress estimation for the Bukov URF – Phase II modelling.

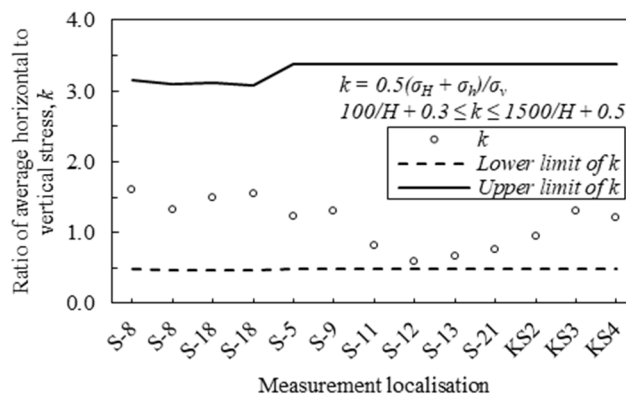
Figure 2.3 plots the ratios of average horizontal stress $(\sigma_H + \sigma_h)/2$ to vertical stress σ_v from the selected measurements compared with the ratio limits suggested by Brown and Hoek (1978). It is clear that all the data lie within the boundary limit, suggesting the reliability of the measurement data to a great extent.

Table 2.2 Estimated quality parameters of Bukov URF – Phase II rock mass for the calculation of *GSI*.

BZ-XIIJ access gallery (mapped approx. 220 m, evaluated approx. 650 discontinuities)				
	<i>RQD</i> (%)		<i>GSI</i> (from Eq. 2.1)	<i>GSI</i> (from Eq. 2.2)
<i>JCond</i> ₈₉	24.7	60	67.1	64.2
<i>J_r</i>	2.30	70	72.1	69.2
<i>J_a</i>	1.21	80	77.1	74.2
Main laboratory tunnel BZ ₁ -XII (mapped approx. 90 m, evaluated approx. 273 discontinuities)				
	<i>RQD</i> (%)		<i>GSI</i> (from Eq. 2.1)	<i>GSI</i> (from Eq. 2.2)
<i>JCond</i> ₈₉	24.5	60	66.8	62.7
<i>J_r</i>	2.13	70	71.8	67.7
<i>J_a</i>	1.26	80	76.8	72.7

Table 2.3 Rock mechanical properties for the Hoek-Brown model.

Property	Unit	Value
Geological Strength Index, GSI	–	65
Deformation modulus, E_b	GPa	28
Poisson's ratio, ν	–	0.2
Elastic bulk modulus, K	GPa	15.56
Elastic shear modulus, G	GPa	11.67
Density, ρ	kg/m ³	2700
Hoek-Brown parameter, a	–	0.502
Hoek-Brown parameter, m_b	–	3.816
Hoek-Brown parameter, s	–	0.02
Uniaxial compressive strength for intact rock, σ_{ci}	MPa	147.86
Tensile strength for rock masses, σ^t	MPa	0.8

**Fig. 2.3** Ratios of average horizontal stress to vertical stress lying within the range found by Brown and Hoek (1978).

2.4.1. INTERPRETATION OF IN SITU STRESS DATA

2.4.1.1. VERTICAL STRESS

It has been proved that the vertical stress can be estimated by overburden weight in most cases (Amadei and Stephansson, 1997; Brown and Hoek, 1978; Herget, 1974; Zang and Stephansson, 2010). In the region of interest, no apparent geological anomalies for example young tectonics, volcanism or rough topography exist. Hence, the vertical stress was estimated through theoretical calculation:

$$\sigma_v = \rho g H \quad (2.3)$$

where, ρ is the average density of rock given as 2700 kg/m³, g is gravity i.e. 9.8 N/kg, and H is depth (550 m).

Note that the vertical stress measured from CCBO method is predominantly lower compared with the theoretically calculated value (i.e. 14.6 MPa), possibly due to over-coring-induced microcracking and mining-induced fractures.

In general, the role vertical stress plays in the *in situ* stress tensor can be roughly estimated based on the major fault patterns (thrust, strike-slip, or normal) in the region (Anderson, 1905). However, complex tectonic structures exist in the planned Bukov URF –

Phase II region, and different fault zones crosscut each other, often have been repeatedly reactivated and thus the fault planes often bear several generations of striation (Bukovská et al., 2019). Clear determination of primary kinematics is therefore nearly impossible. Hence, it is very difficult to determine whether the vertical stress acts as maximum, intermediate or minimum principal stress in this region, due to the occurrence of complex geological structures.

2.4.1.2. HORIZONTAL STRESSES

Since the *in situ* stress characteristics are compiled from multiple methodologies, it is impracticable to rigorously assign errors purely using statistical methods. In addition, the measurement data show significant scatter. Hence, it is better to estimate the state of stress on the trends in the data rather than on individual test results. The ratio between the maximum and intermediate principal stress (R_1) and the mean principal stress (M) were adopted to back-calculate the stress magnitudes (Martin, 2007), instead of directly taking the average values of each stress components. As a result, three different *in situ* stress scenarios could be derived, depending on the role the vertical stress plays, as summarised in Table 2.5.

Table 2.4 Detailed *in situ* stress measurement data (Bukovská et al., 2020; Souček et al., 2018).

Localization	Method	Depth	S_v – theoretical/ <i>measured</i>	S_H	S_h	S_H orientation (°)	Ratio $S_v:S_H:S_h$		
GS20/1	BB	907	24.0	–	–	177	–	–	–
GS20/1	BB	916	24.3	–	–	175	–	–	–
GS20/1	BB	921	24.4	–	–	150	–	–	–
GS20/1	BB	936	24.8	–	–	170	–	–	–
GS20/2	BB	932	24.7	–	–	170	–	–	–
GS20/1	BB	907	24.0	–	–	177	–	–	–
S-8	HF	565	15.0	31	17	180	1.0	2.1	1.1
S-8	HF	578	15.3	27	13.5	21	1.0	1.8	0.9
S-18	HF	575	15.2	29.3	15.9	30	1.0	1.9	1.0
S-18	HF	583	15.4	31.5	16.5	28	1.0	2.0	1.1
S-5	CCBO	520	<u>5.7</u>	8.1	5.9	80	1.0	1.4	1.0
S-9	CCBO	520	<u>7.0</u>	15.4	2.9	15	1.0	2.2	0.4
S-11	CCBO	520	<u>10.6</u>	10.1	7.2	15	1.0	1.0	0.7
S-12	CCBO	520	<u>13.9</u>	11.2	5.3	30	1.0	0.8	0.4
S-13	CCBO	520	<u>14.8</u>	14.6	5.1	228	1.0	1.0	0.3
S-21	CCBO	520	<u>7.9</u>	7	4.9	228	1.0	0.9	0.6
KS2	RCA	520	13.8	16.5	9.6	30	1.0	1.2	0.7
KS3	RCA	520	13.8	31.7	4.1	41	1.0	2.3	0.3
KS4	RCA	520	13.8	30.3	2.8	41	1.0	2.2	0.2

Note: S_v – vertical rock mass stress component; S_H – major horizontal rock mass stress component; S_h – minor horizontal rock mass stress component; GS20/1 – geotechnical station situated on the level 20 of the Rožná mine (Bukovská et al., 2020); S-5, S-8, S-9, S-11, S-12, S-13, and S-18 – boreholes evaluated within the Bukov URF – Phase I construction (Bukovská et al., 2020; Bukovská et al., 2019); KS2, KS3, and KS4 – convergence stations with convergence measurements used for reverse analysis of the rock mass stress state assessment (Bukovská et al., 2019; Souček et al., 2018).

Table 2.5 Three different scenarios of *in situ* stress states depending on the role of the vertical stress.

Scenarios	Maximum principal stress, σ_1	Intermediate principal stress, σ_2	Minimum principal stress, σ_3
I: $\sigma_3 = \sigma_v$	$R_1(3M - \sigma_v)/(1 + R_1)$	$R_1(3M - \sigma_v)/(1 + R_1)$	σ_v
II: $\sigma_2 = \sigma_v$	$R_1\sigma_v$	σ_v	$3M - (1 + R_1)\sigma_v$
III: $\sigma_1 = \sigma_v$	σ_v	σ_v/R_1	$3M - (1 + 1/R_1)\sigma_v$

Table 2.6 Statistical data of mean principal stress and principal stress ratios.

Data analysis	Mean	Standard deviation
Mean principal stress, M	13.8 MPa	5.4 MPa
Principal stress ratio $R_1: \sigma_1/\sigma_2$	1.62	0.47
Principal stress ratio $R_2: \sigma_1/\sigma_3$	3.37	2.91

Based on Table 2.4, the average values and standard deviations of each parameter are shown in Table 2.6.

From the measurement results it can be stated that the rock mass is relatively complicated in terms of the orientation and magnitude of the stress field. The local variability of the interpreted results is manifested mainly in the orientation. The global evaluation of the whole group of current and previously performed measurements shows the orientation of the main component of horizontal stress (S_H) is in the direction of NW–SE to N–S, but the directions NNE–SSW are

not exceptional either. Hence, the maximum horizontal stress orientation was simplified as N–S.

2.4.2. POSSIBLE SCENARIOS OF IN SITU STRESS STATE

The rock mass behaviour and stability of the Bukov URF – Phase II was then investigated at the most probable cases of *in situ* stress states based on Tables 2.5–2.6, with the mean stresses and principal stress ratios ranging by either-side one standard deviation. Considering that the ratio R_1 ranges from 1.15 to 2.09, four different levels of R_1 (1.2, 1.4, 1.6,

Table 2.7 Simulation scenarios of different *in situ* stress states.

Scenarios	Subcase	$R_1 = \sigma_1/\sigma_2$	σ_1	σ_2	σ_3	M	a_s
I	#1	1.2	22.9	19.1		18.9	0.3717
	#2	1.4	24.5	17.5			0.3850
	#3	1.6	25.8	16.1	14.6		0.4055
	#4	1.8	27.0	15.0			0.4223
II	#1	1.2	17.5		13.8	15.3	0.3294
	#2	1.4	20.4		10.9		0.3716
	#3	1.6	23.4	14.6	7.9		0.4448
	#4	1.8	26.3		5.0		0.5627
III	#1	1.2		12.2	2.6	9.8	0.4995
	#2	1.4		10.4	4.4		0.3514
	#3	1.6	14.6	9.1	5.7		0.2763
	#4	1.8		8.1	6.7		0.2350

and 1.8) was selected while keeping the mean stress M constant for each scenario. The corresponding values of the three principal stresses in each subcase are listed in Table 2.7.

3. NUMERICAL SIMULATION

3.1. MODEL GENERATION AND BOUNDARY CONDITIONS

The Itasca software FLAC3D (Itasca Consulting Group, 2012) was adopted to analyse the stability of the planned underground research facility. The well-known Hoek-Brown model was employed to control the rock mass behaviour in this project. The failure mode was assumed as ductile failure (elastic-perfectly plastic) for a preliminary evaluation of the overall stability. The material properties σ_{ci} , m_b , s and a were assumed to remain constant after the onset of plastic yield, as shown in Table 2.3.

The model is fixed on the bottom boundary while free on the top and side boundaries. A vertical stress $\sigma_v = 14.6$ MPa is applied on the top surface. The maximum horizontal stress points north which coincides with the positive y-direction of the current model, and the minimum horizontal stress is applied in the x-direction. In terms of the horizontal stress magnitudes, three different scenarios with each having four levels of the principal stress ratio R_1 were studied, as shown in Table 2.7.

The model dimension was determined carefully to eliminate the boundary effect. The top and bottom boundary of the model were set as ten excavation height away from the excavation periphery (Itasca Consulting Group, 2012), i.e. the model has a height of 84 m. To select the appropriate lateral boundary dimension, a series of parallel model (Fig. 3.1) with different values of width/length were generated. All the designed roadways and laboratory chambers were excavated simultaneously and run to equilibrium. Instead of using the Hoek-Brown model and complex *in situ* stress conditions, the conventional

Mohr-Coulomb model was adopted for investigating the boundary effect, and the boundary stress condition is simply determined as

$$\sigma_H = \sigma_h = \sigma_v v / (1 - v) \quad (3.6)$$

where σ_H and σ_h are the maximum and minimum horizontal stress, respectively, and the passion ratio v is given as 0.2.

Figure 3.2 shows the change of maximum displacement magnitude of the models with varying lateral boundary dimensions. It is clear that the lateral boundary effect on the model displacement is minor. The variation of the maximum displacement magnitude is within 1 mm when the lateral distance between the boundaries and the excavation region increased from 50 m to 300 m. Considering the calculation efficiency, $L = 50$ m was selected and a corresponding dimension of $224 \times 336 \times 84$ m was finally determined for the 3D model. A total of 583,233 zones are contained in the model, with the unit zone volume ranging from 8.5 cm^3 to 130 m^3 . To ensure the continuity of model behaviour between different sub-grids, the “interface” element was applied to connect the adjoining primitive shapes having different zone size / face shape. Both the normal and shear stiffness were set as 10 times the apparent stiffness of the adjoining zone i.e. $\max[(K + 4G/3)/\Delta z_{\min}]$ according to the FLAC3D manual (Itasca consulting group, 2012), where K and G are the bulk and shear moduli, respectively, and Δz_{\min} is the smallest width of an adjoining zone in the normal direction, with the tensile strength given as a very high value of 10 GPa.

3.2. MODELLING PROCEDURE

The modelled roadways and chambers were excavated step by step. As shown in Figure 3.3, the excavation includes ten sequences. Firstly, the main roadway remained from previous mining works were excavated. The roadway branch in the furthest south

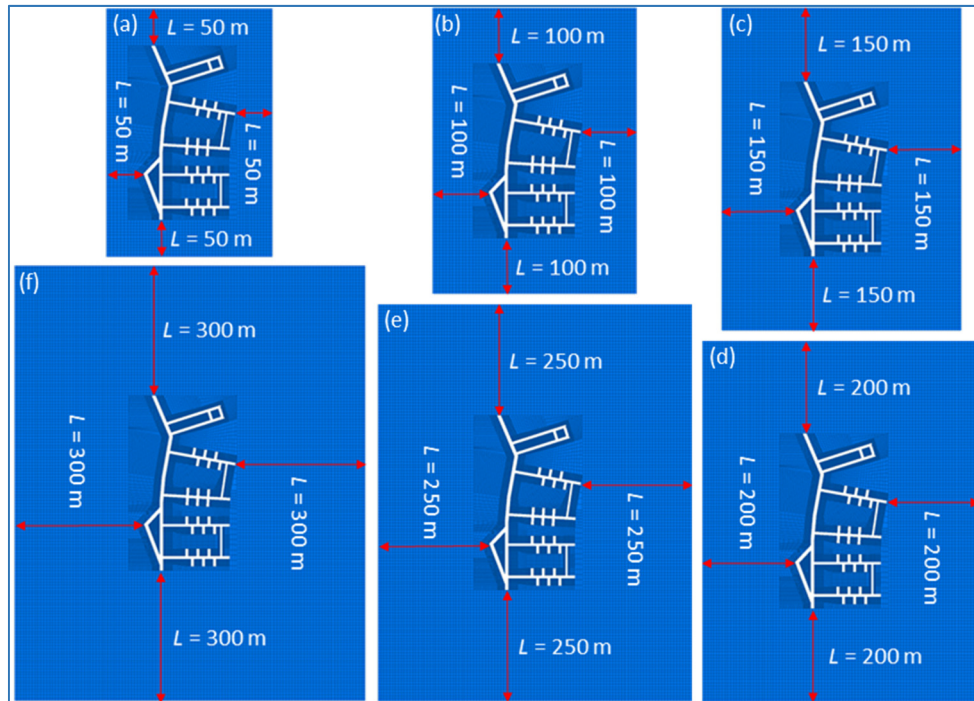


Fig. 3.1 Plane view of the model geometry with different lateral boundary dimensions.

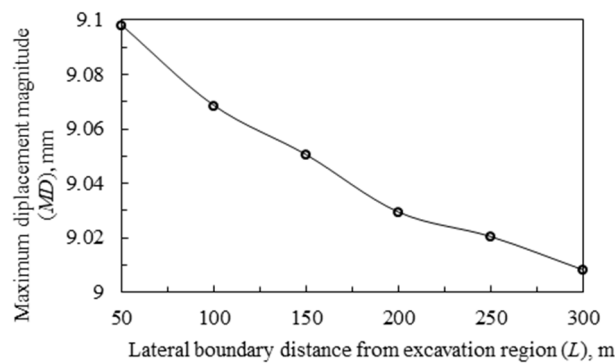


Fig. 3.2 Lateral boundary effect on the maximum displacement magnitude after a whole-stage excavation.

part (RoadwayL8) were then excavated, followed by the next branch the northern vicinity (RoadwayL7), and a ventilation roadway (Ventilation7–8) connecting these two branches was developed afterwards. Next, the excavation of the third and fourth branches (RoadwayL6 and RoadwayL5, respectively) were conducted, following the second ventilation roadway (Ventilation5–6) later on. After that, the last group of roadways and chambers (RoadwayL4) were excavated sequentially, as depicted in Figure 3.3. The model was run to equilibrium after each sequence. Both velocity and displacement of the whole model were reset to zero after the main roadway excavation, so that the net increments resulted from the new excavations can be directly observed. All the codes and FISH subroutines during the modelling can be provided by request.

3.3 MODELLING RESULTS AND DISCUSSION

3.2.1. MINIMUM STRENGTH-STRESS RATIO AND MAXIMUM DISPLACEMENT MAGNITUDE

As with all other engineering projects, the FoS is the most common index evaluating the feasibility of the construction design and the stability of the rock mass surrounding the excavations. In the case of underground tunnel excavation, conventional parameters calculating the factor-of-safety index include the current stress state's proximity to failure, and displacement or convergence compared with a specified threshold. The minimum strength-stress ratio (*MSR*) and the maximum displacement magnitude (*MD*) inside the whole model were hence analysed.

As shown in Figure 3.4, the value of *MSR* varies considerably as the model-input *in situ* stress state changes, ranging from 1.08 to 1.56. However, due to

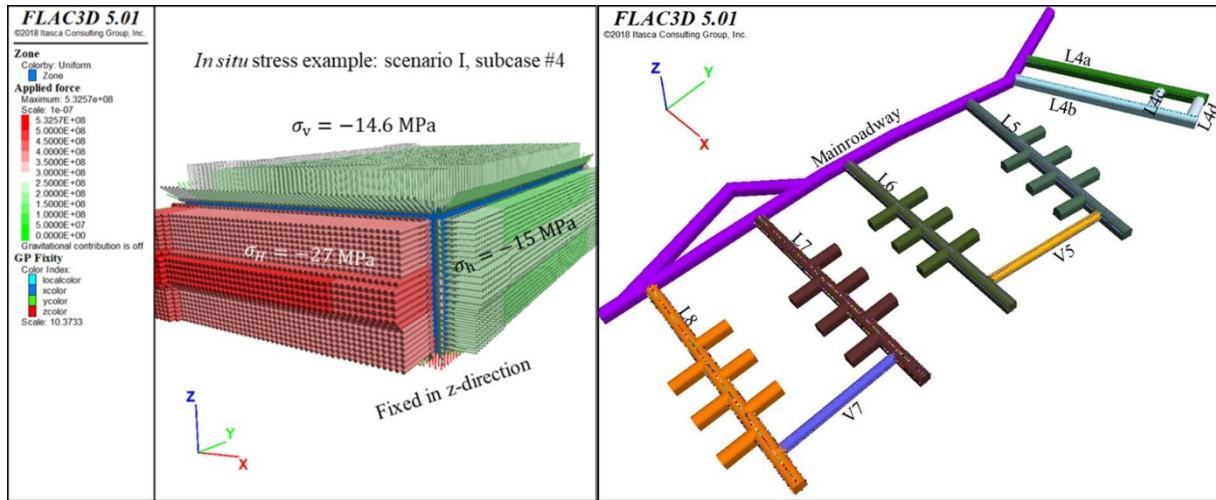


Fig. 3.3 Model generation and excavation sequences of the designed underground research facility.

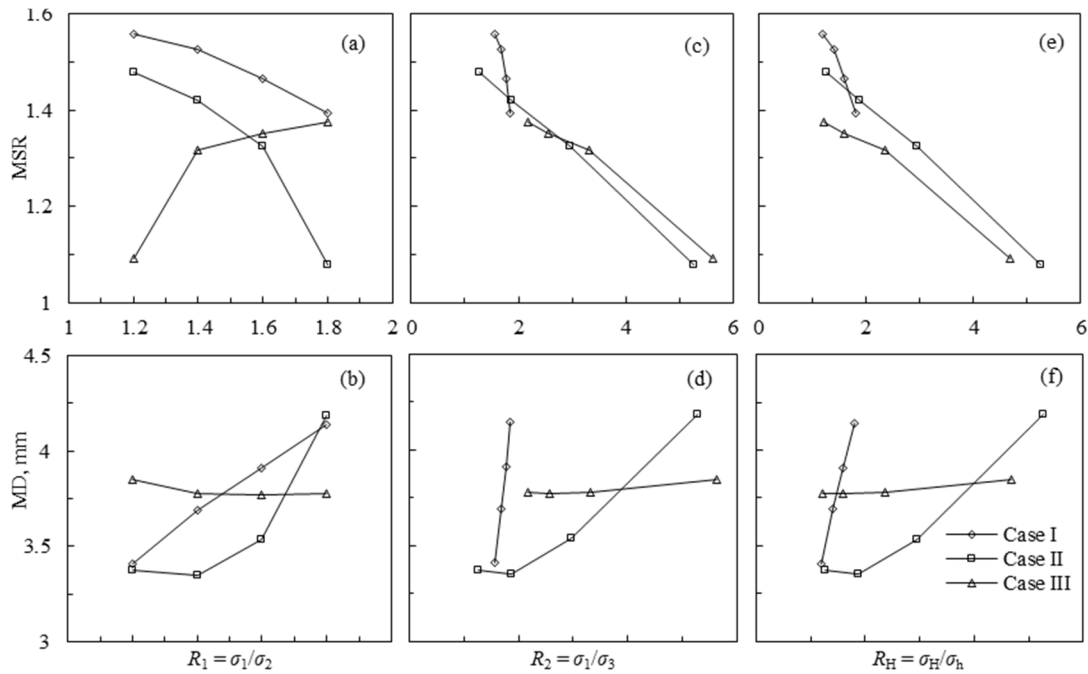


Fig. 3.4 Minimum strength-stress ratio and maximum displacement magnitude vs. principal stress ratios under different *in situ* stress conditions.

the strength-stress ratio larger than unity and the high modulus of rock masses, the displacement magnitude varies only within 1 mm, and 4.2 mm maximum. In case I where the vertical stress acts as the minimum principal stress, *MSR* decreases gradually as R_1 (i.e. σ_1/σ_2) increases, whereas *MD* increases accordingly. The same trend goes for case II where the vertical stress plays the role of intermediate principal stress. However, *MSR* increases with the increase of R_1 and *MD* decreases slightly in case III, where the maximum component of the *in situ* stress tensor is vertical. On the other hand, the variation trends of *MSR* and *MD* respectively are consistent in all cases when plotted against the principal stress ratio R_2 (σ_1/σ_3) and the

horizontal stress ratio R_H (σ_H/σ_h). As shown in Figure 3.4 (c–f), the value of *MSR* decreases while *MD* increases in all three scenarios, when R_2 and R_H increase. This is understandable as the increased R_2 or R_H lead to either the increase in σ_1 (case I and II) or the decrease in σ_3 (case III). According to the Hoek-Brown criterion as depicted in Eq. (3.7), the decrease in σ_3 causes the drop in the compressive strength σ_{1m} of the rock mass. Either an increase in σ_1 or decrease in σ_3 results in decreased σ_{1m}/σ_1 i.e. the strength-stress ratio. On the other hand, the increase in R_1 causes increased σ_1 in case I where σ_3 remains constant, increased σ_1 in case II where σ_3 decreases, and increased σ_3 in case III where σ_1 remains constant.

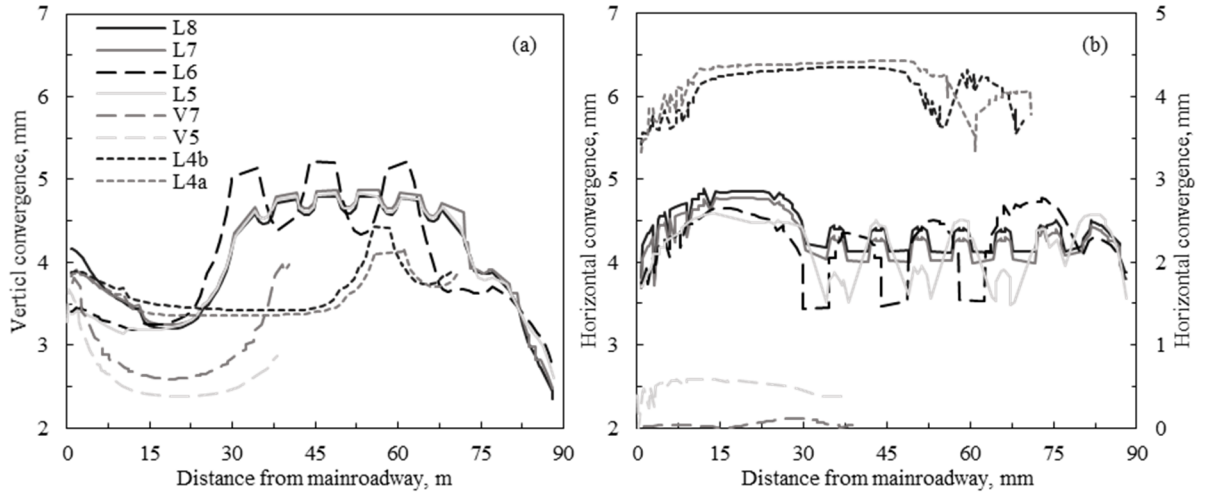


Fig. 3.5 Roadway convergence distribution in case I with $R_1 = 1.2$.

Note: curves in (b) for ventilation channels (V7 and V5) and the major roadways L4(a–b) are plotted against the right-side (secondary) y-axis for the purpose of distinct demonstration.

As a consequence, the variations of MSR and MD in case III show ‘abnormal’ trends with increased R_1 , as plotted in Figures 3.4(a–b).

$$\sigma_{1m} = \sigma_3 + \sigma_{ci} \left\{ m_b \frac{\sigma_3}{\sigma_{ci}} + s \right\}^a \quad (3.7)$$

In addition, with the drops of the mean stress M , the absolute value of the curve slope also decreases in terms of both MSR and MD , largely depending on the varying trends of the *in-situ* stress dominated σ_{1m}/σ_1 at different M levels. This suggests that the influence of R_2 or R_H on the excavation stability is more significant at higher mean stress levels.

3.2.2. DISTRIBUTION OF CONVERGENCE AND STRENGTH-STRESS RATIO ALONG ROADWAYS

To further evaluate the roadway deformation and stability, a series of measurement points were selected on the roadway surface. Four points were chosen in each cross section perpendicular to the roadway axis, located on the roof, floor, left and right ribs respectively, with a cross section interval of roughly 0.5 m. A total of 4556 points were measured, demonstrated as sphere marks in Figure 3.3 (right). The statistical distribution of the horizontal/vertical convergence and the strength-stress ratio were analysed. Since vertical stress keeps constant in all the modelling scenarios, and the horizontal stress ratio R_H has more consistent influence on the FoS related roadway parameters according to the results mentioned above, only R_H is adopted for the analysis in this section.

3.2.2.1. CONVERGENCE

Various researchers have adopted convergence indices to judge the failure or ultimate/serviceability limit state of the excavation (e.g. Heidarzadeh et al., 2021; Zhang and Mitri, 2008; Abdellah et al., 2018). Convergence ratio i.e. the ratio of convergence to the original span of the excavation is commonly employed

as the stability criterion. According to the modelling results, the maximum horizontal/wall convergence ratio is 0.18 %, while the maximum vertical convergence ratio is 0.15 %, which are considered satisfactory in the current project.

(1) The influence of roadway layout on the convergences

Modelling results reveal that the qualitative distribution patterns of convergences depend on the roadway layout characteristics, remaining similar regardless of the changes of *in situ* stress states. In other words, the excavation-induced stress concentration/release state instead of the *in situ* stresses dominates the roadway convergence patterns. Figure 3.5 shows the distribution patterns of the roadway convergence in case I ($R_1 = 1.2$). Major roadways (i.e. L8, L7, L6, L5 and L4) show curves with troughs and crests along the roadway axes due to intersections with perpendicular chambers. Ventilation channels (i.e. V7 and V5) reveal concave/convex type curves instead. Roadways connected with more numbers of chambers generally have larger convergence, with maximum vertical convergences and minimum horizontal convergences in each roadway located in close proximity to the roadway-chamber intersections. Note that the pattern for the roadway L6 is different from other major roadways due to different chamber layout. In L6, the chambers are symmetrically placed, causing slightly higher vertical convergence at the intersection.

Figure 3.6 plots the maximum value of both vertical and horizontal convergence of each roadway against the horizontal stress ratio R_H at three different *in situ* stress scenarios. With the increase of R_H , the maximum vertical convergence decreased in roadways perpendicular or with larger angle to the direction of maximum horizontal stress (i.e. Y-axis of the model). In ventilation channels where the roadway axis has small angle to the model Y-axis, the trend is opposite. However, the increase of R_H has a consistent

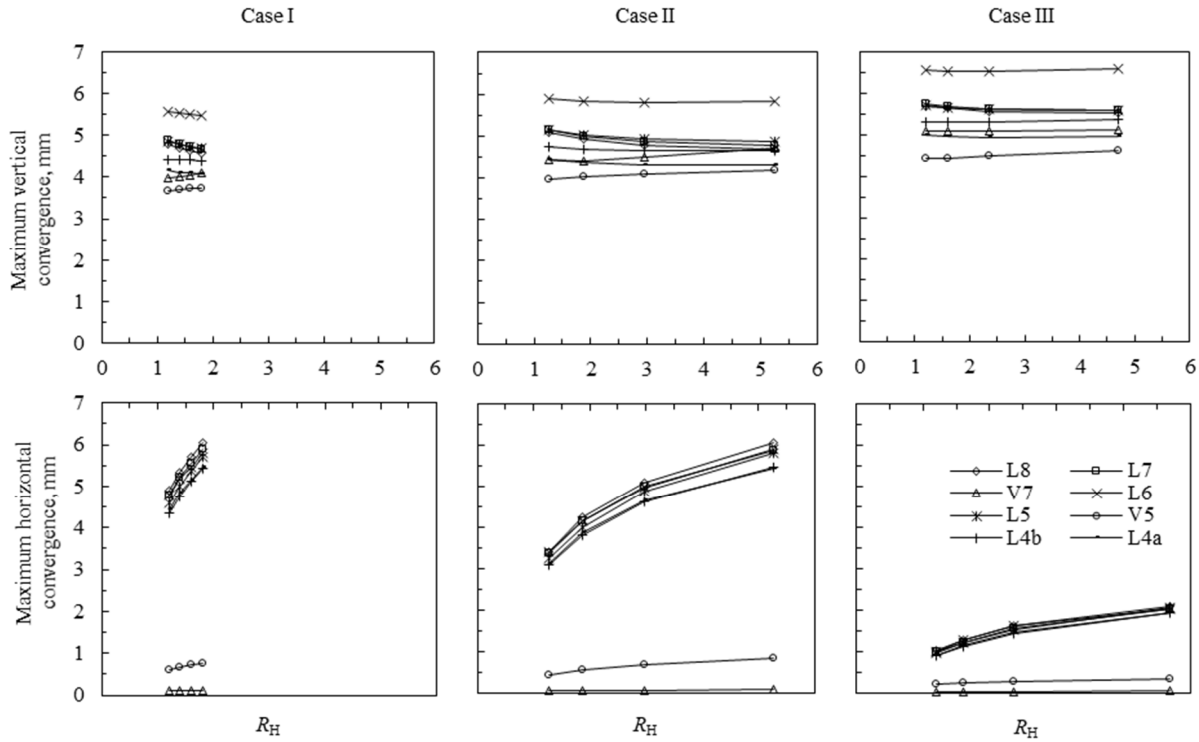


Fig. 3.6 Maximum convergences of each roadway vs. horizontal stress ratios at different *in situ* stress conditions.

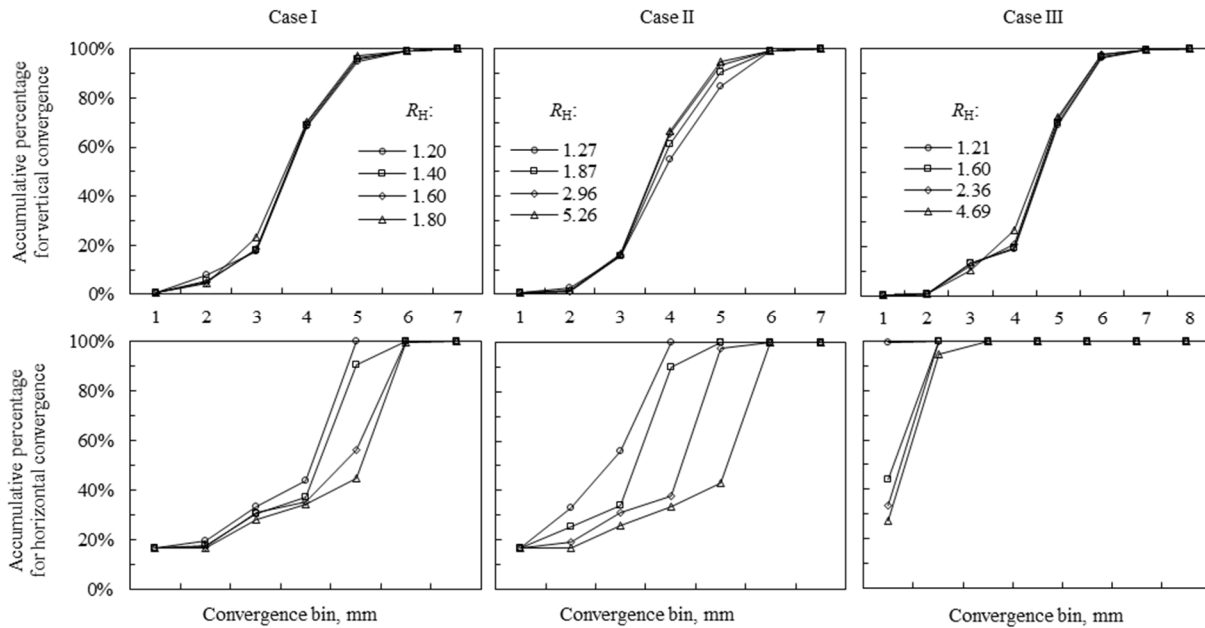


Fig. 3.7 Accumulated percentage curves of roadway convergences at different *in situ* stress conditions.

increasing impact on the maximum horizontal convergence for all roadways. Ventilation channels have minor horizontal convergence, mainly because their axes are mostly parallel to the maximum horizontal stress. With the decrease of the mean stress M , i.e. with vertical stress transferred from minimum principal stress to intermediate to maximum principal stress, such influences of R_H on both the vertical and horizontal convergence becomes minor. In addition, as the mean stress M falls, the general magnitude of the

roadway maximum vertical convergence rises while the maximum horizontal convergence drops. Furthermore, the influences of both R_H and M on the horizontal convergence are more significant than those on the vertical convergence.

(2) The influence of R_H on the cumulative distribution of roadway convergence

The convergence data of all the roadways calculated based on the measurement points on the roadway surface were then statistically analysed for

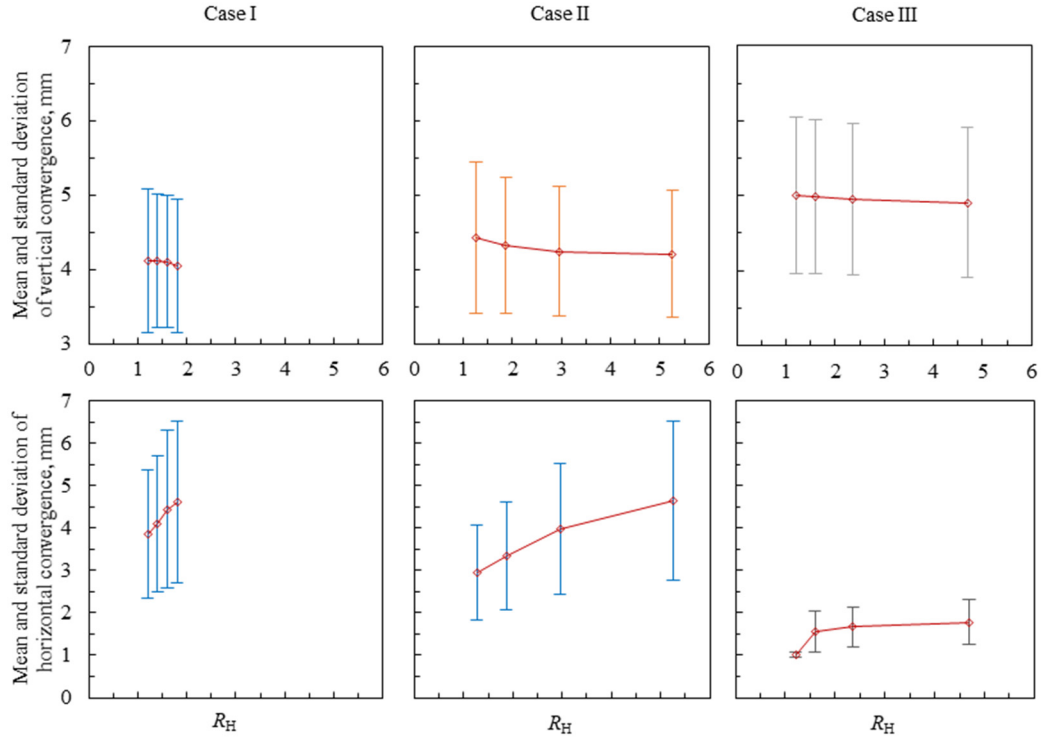


Fig. 3.8 Mean and standard deviation of the convergence data at different *in situ* stress conditions.

each *in situ* stress condition. The cumulative distributions of the roadway convergence were plotted against a series of convergence bin, as shown in Figure 3.7. Generally for each case, the horizontal convergence curve drops with the increase of R_H , and the curves have larger variation when R_H changes within a broader range. That is to say, the stronger anisotropic stress field causes higher accumulative percentages for larger horizontal convergence magnitude, increasing the overall roadway deformation. On the other hand, the cumulative distribution of vertical convergence varies insignificantly at the change of R_H , mainly because both the mean stress and the vertical stress remain constant at the same case, while the horizontal stress ratios and magnitudes change considerably.

Both the mean and standard deviation of the convergence data were further analysed, as plotted in Figure 3.8. It can be seen that with the increase of R_H , both mean and standard deviation of vertical convergence data decreased, while those of horizontal convergence data increased, since most parts of the excavations are nearly perpendicular to the orientation of σ_H . The changing rate of horizontal convergence mean and standard deviation is much larger than vertical convergence at the same modelling case, as the vertical stress remains constant during the change of R_H . With the decrease of the mean stress M , the vertical convergence increased while horizontal convergence decreased, as the magnitude ranges of σ_H also declined. At lower levels of the mean stress M , the curve slope decreased, or rather the influence of R_H reduced.

3.2.2.2. STRENGTH-STRESS RATIO

Both the cumulative distribution curves and the normal density distributions of the strength-stress ratio measured along the roadways were plotted in Figure 3.9. With the increase of the principal stress ratio R_H , the cumulative distribution curve is higher while both the mean and the variance of the strength-stress ratio decreased in all three cases, meaning that the overall safety and stability of the roadways decreased.

An empirical stability model was also proposed to describe the cumulative distribution curves of the roadway strength-stress ratio:

$$P = [(a_s \cdot R_s)^{1/(1-b)} + 1]^{-b} \quad (3.8)$$

where, P is accumulative percentage of the strength-stress ratio R_s , and a_s and b are fitting parameters. a_s is a stability parameter related to the horizontal stress ratio R_H and the mean stress M .

$$a_s = \alpha R_H + \beta M + \gamma \quad (3.9)$$

where, α , β , and γ are fitting parameters, and M is mean *in situ* stress.

Given that a small number of samples were used to fit the cumulative distribution curves, the generalised instead of ordinary least squares method was used to recover the full uncertainty, considering the effect of covariance matrix. Predicted curves according to Equation (3.8) are shown in Figure 3.9 together with the values of fitting parameters as well as the original statistical data ($R^2 = 0.96$). This is very interesting, as the overall stability of the excavations

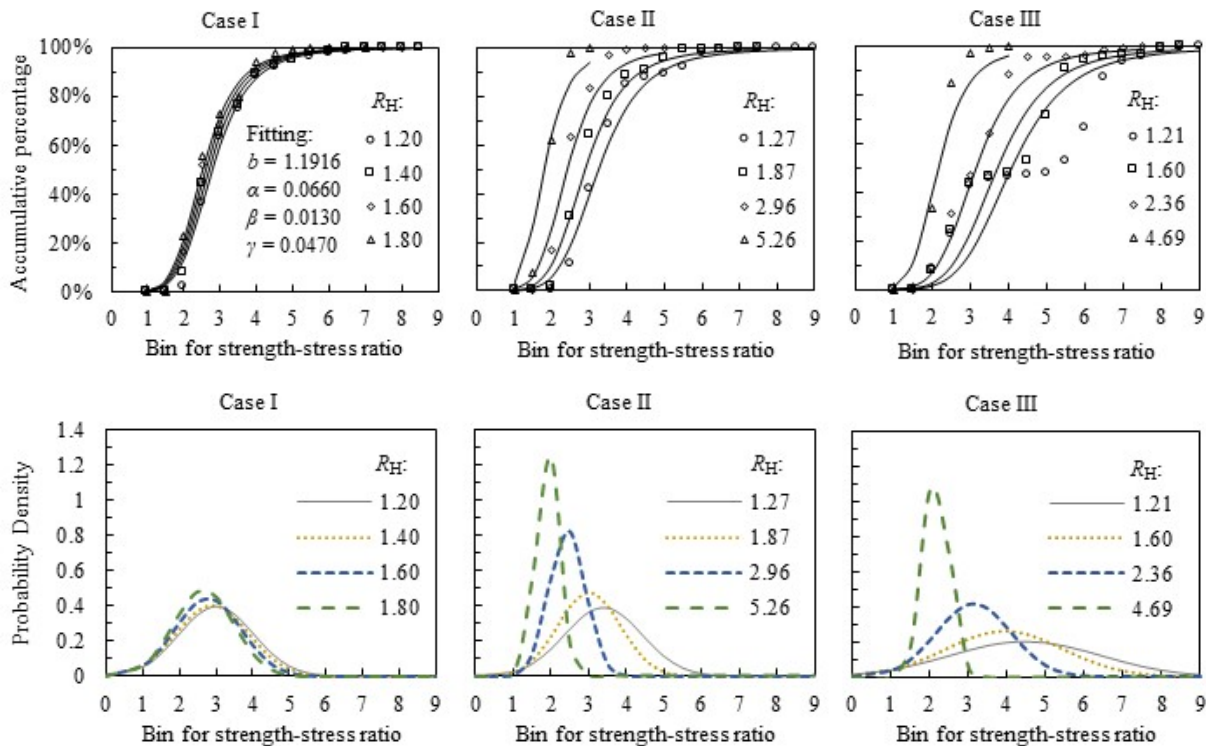


Fig. 3.9 Accumulated percentage and probability density curves of strength-stress ratio at different *in situ* stress conditions.

with complicated configurations can thus be quantitatively evaluated. The mean stress and the horizontal stress ratio are mainly focused on as two of the most important parameters controlling the URF stability. The stability parameter a_s mathematically combines these two parameters, while representing a clear physical meaning i.e. the overall stability or the potential of failure. The smallest value of a_s in all twelve modelling conditions represents the most favourable case (scenario III, subcase #4) among the listed *in situ* stress scenarios in Table 2.7. As in most cases underground excavations have complicated geometry layout and configuration, one single value e.g. the peak convergence or minimum strength-stress ratio cannot accurately describe the worst condition. The proposed stability model provides a better but simple mathematical model to comprehensively evaluate the situation, and offers a reference point for stability analysis and layout planning optimisation in similar conditions.

4. SUMMARY AND CONCLUSIONS

This paper studied the influence of different pre-excavation *in situ* state of stress on the deformation and strength-stress ratio of the planned Bukov URF – Phase II in Czech Republic using the numerical software FLAC3D. The Hoek-Brown criterion was adopted to simulate the constitutive behaviour of the rock mass. Corresponding geomechanical properties of the rock mass was estimated by combining field geological mapping, laboratory experiments and theoretical calculation. The most probable conditions

of the *in situ* stress were derived by back calculation from the normal distributions of the mean principal stress and principal stress ratios instead of a direct average of the *in situ* stress components. The model was run on three scenarios and totally twelve subcases. Both the displacement/convergence and the strength-stress ratio of the URF excavation were focused on for the sensitivity and stability analysis. Modelling results show that both the *in situ* stress state and excavation/layout-induced stress redistribution jointly influence the deformation and stability of the URF. The significance and necessity of careful treatment of the *in situ* stress data in numerical modelling was highlighted. Important conclusions are drawn as follows:

(1) The influence of the horizontal stress ratio R_H and the mean stress M on the stability of the Bukov URF – Phase II was analysed from several different perspectives, including the global model parameters i.e. the minimum strength-stress ratio (MSR) and the maximum displacement magnitude (MD), the individual roadway parameters i.e. the maximum horizontal and vertical convergence, and the cumulative distribution curves of both the convergences and the strength-stress ratio collected along all the roadways. Results indicated that the increased horizontal stress anisotropy and the mean stress level jointly increase the overall deformation and lower the URF safety and stability condition. Such influences on the horizontal convergence are more considerable than those on the vertical convergence.

(2) A novel empirical stability model was proposed to describe the cumulative distribution of the strength-stress ratio along all the roadways with complex layout, and takes into account both R_H and M . The stability parameter a_s in the model is defined to have clear physical meaning, which quantitatively describes the overall stability of the URF with complicated configuration.

Future detailed geotechnical monitoring during and after the excavation of Bukov URF Phase II is essential to validate the adopted Hoek-Brown model where some assumptions are made e.g. the ignorance of the intermediate principal stress and rock anisotropy, and to refine the numerical modelling and contribute to the design and construction of the next-stage national nuclear waste repository in Czech Republic. In addition, the proposed stability model needs further validation in similar tunneling and underground excavation projects to verify its mathematical ubiquity.

ACKNOWLEDGEMENT

This work was supported by the Czech Radioactive Waste Repository Authority [grant number 4.1.5.1/ESS:SURAO-2014-2304] and the Czech Academy of Sciences [grant number RVO: 68145535]. The authors thank the Czech Radioactive Waste Repository Authority for permission to publish this work. The first author was supported by the Program to support prospective human resources – post Ph.D. candidates in the Czech Academy of Sciences.

REFERENCES

- Abdellah, W.R., Ali, M.A. and Yang, H.S.: 2018, Studying the effect of some parameters on the stability of shallow tunnels. *J. Sustain. Min.*, 17, 1, 20–33. DOI: 10.1016/j.jsm.2018.02.001
- Amadei, B. and Stephansson, O.: 1997, Rock stress and its measurement. Springer, Dordrecht, 23–120. DOI: 10.1007/978-94-011-5346-1
- Anderson, E.M.: 1905, The dynamics of faulting. *Trans. Ed. Geol. Soc.*, 8, 387–402. DOI: 10.1144/transed.8.3.387
- Apted, M.: 2019, Underground research laboratories: purposes, evolution of objectives, and brief history. U.S. Nuclear Waste Technical Review Board. <https://www.nwtrb.gov/docs/default-source/meetings/2019/april/apted.pdf?sfvrsn=6>.
- Apted, M.J. and Ahn, J.: 2017, Geological repository systems for safe disposal of spent nuclear fuels and radioactive waste (2nd ed.). Woodhead Publishing, Sawston Cambridge, 3–26. DOI: 10.1016/B978-0-08-100642-9.12001-8
- Barton, N., Lien, R. and Lunde, J.: 1974, Engineering classification of rock masses for the design of tunnel support. *Rock Mech. Rock Eng.*, 6, 4, 189–236. DOI: 10.1007/BF01239496
- Bieniawski, Z.T.: 1989, Engineering rock mass classifications: a complete manual for engineers and geologists in mining, civil, and petroleum engineering. John Wiley & Sons, New York, 54–58.
- Brady, B.H.G. and Brown, E.T.: 2007, Pre-mining state of stress. In: *Rock Mechanics for underground mining* (3rd ed.). Springer, Dordrecht, 142–164. DOI: 10.1007/978-1-4020-2116-9_5
- Brown, E.T. and Hoek, E.: 1978, Trends in relationships between measured in-situ stresses and depth. *Int. J. Rock Mech. Min. Sci. Geomech. Abstr.*, 15, 4, 211–215. DOI: 10.1016/0148-9062(78)91227-5
- Bukovská, Z. et al.: 2020, Data acquisition from the deep horizons of the Rožná Mine. RAWRA Technical Report (No. 464/2020/ENG). Czech Radioactive Waste Repository Authority, Prague, 48 pp.
- Bukovská, Z., Soejono, I., Vondrovic, L., Vavro, M., Souček, K., Buriánek, D., Dobeš, P., Švagera, O., Waclawik, P. and Řihošek, J.: 2019, Characterization and 3D visualization of underground research facility for deep geological repository experiments: A case study of underground research facility Bukov, Czech Republic. *Eng. Geol.*, 259, 105186. DOI: 10.1016/j.enggeo.2019.105186
- Corkum, A.G., Damjanac, B. and Lam, T.: 2018, Variation of horizontal in situ stress with depth for long-term performance evaluation of the Deep Geological Repository project access shaft. *Int. J. Rock Mech. Min. Sci.*, 107, 75–85. DOI: 10.1016/j.ijrmms.2018.04.035
- Delay, J., Bossart, P., Ling, L.X., Blechschmidt, I., Ohlsson, M., Vinsot, A., Nussbaum, C. and Maes, N.: 2014, Three decades of underground research laboratories: what have we learned? *Geol. Soc. London Spec. Publ.*, 400, 1, 7–32. DOI: 10.1144/SP400.1
- Feiveson, H., Mian, Z., Ramana, M.V. and von Hippel, F.: 2011, Managing nuclear spent fuel: Policy lessons from a 10-country study. *Bull. At. Sci.* <https://thebulletin.org/2011/06/managing-nuclear-spent-fuel-policy-lessons-from-a-10-country-study>.
- Haimson, B.C. and Cornet, F.H.: 2003, ISRM suggested methods for rock stress estimation—part 3: hydraulic fracturing (HF) and/or hydraulic testing of pre-existing fractures (HTPF). *Int. J. Rock Mech. Min. Sci.*, 40, 7–8, 1011–1020. DOI: 10.1016/j.ijrmms.2003.08.002
- Heidarzadeh, S., Saeidi, A. and Rouleau, A.: 2021, The damage-failure criteria for numerical stability analysis of underground excavations: A review. *Tunn. Underg. Space Technol.*, 107, 103633. DOI: 10.1016/j.tust.2020.103633
- Herget, G.: 1974, Ground stress determinations in Canada. *Rock Mechanics*, 6, 1, 53–64. DOI: 10.1007/BF01238053
- Hoek, E., Carter, T.G. and Diederichs, M.S.: 2013, Quantification of the geological strength index chart. In: *Pyrak-Nolte, Chan, A., Dershowitz, W., Morris, J. and Rostami J. (Eds.): 47th US Rock Mechanics/Geomechanics Symposium*, San Francisco, CA, 1757–1764.
- Hudson, J.A., Cornet, F.H. and Christiansson, R.: 2003, ISRM Suggested methods for rock stress estimation—Part 1: Strategy for rock stress estimation. *Int. J. Rock Mech. Min. Sci.*, 40, 7–8, 991–998. DOI: 10.1016/j.ijrmms.2003.07.011
- Itasca Consulting Group: 2012, FLAC3D 5.0 manual. Itasca Consulting Group, Minneapolis.
- Kříbek, B. and Hájek, A.: 2005, Rožná uranium deposit: model of late Variscan and post Variscan

- mineralizations. Czech Geological Survey, Prague, 15 pp., (in Czech).
- Laverov, N.P., Yudinsev, S.V., Kochkin, B.T. and Malkovsky, V.I.: 2016, The Russian strategy of using crystalline rock as a repository for nuclear waste. *Elements*, 12, 4, 253–256. DOI: 10.2113/gselements.12.4.253
- Martin, C.D.: 2007, Quantifying in situ stress magnitudes and orientations for Forsmark. Forsmark stage 2.2. SKB Report (No. R-07-26), Swedish Nuclear Fuel and Waste Management Co., Stockholm, 71–80.
- Napa-García, G.F., Cámara, T.R. and Torres, V.F.N.: 2019, Optimization of room-and-pillar dimensions using automated numerical models. *Int. J. Min. Sci. Technol.*, 29, 5, 797–801. DOI: 10.1016/j.ijmst.2019.02.003
- NEA-OECD: 2013, Underground research laboratories (URL) (NEA Report No. 78122). <https://www.oecd-neo.org/rwm/reports/2013/78122-rwm-url-brochure.pdf>.
- Patocka, M. and Jaros, M.: 2020, Geological and geotechnical condition of URF Bukov roadways drive – Stage II. DIAMO Technical Report, DIAMO, s.p., 98 pp., (in Czech).
- Peng, S.S., Cheng, J., Du, F. and Xue, Y.: 2019, Underground ground control monitoring and interpretation, and numerical modeling, and shield capacity design. *Int. J. Min. Sci. Technol.*, 29, 1, 79–85. DOI: 10.1016/j.ijmst.2018.11.026
- Ptáček, J., Melichar, R., Hájek, A., Koniček, P., Souček, K., Staš, L., Kříž, P. and Lazárek, J.: 2013, Structural analysis within the Rožná and Olší uranium deposits (Strážek Moldanubicum) for the estimation of deformation and stress conditions of underground gas storage. *Acta Geodyn. Geomater.*, 10, 2, 237–246. DOI: 10.13168/AGG.2013.0024
- Renani, H.R. and Martin, C.D.: 2020, Factor of safety of strain-softening slopes. *J. Rock Mech. Geotech. Eng.*, 12, 3, 473–483. DOI: 10.1016/j.jrmge.2019.11.004
- Rocscience Inc.: 2017, RocData (5.0). <https://www.rocscience.com/help/rocddata>.
- Saeidi, A., Heidarzadeh, S., Lalancette, S. and Rouleau, A.: 2021, The effects of in situ stress uncertainties on the assessment of open stope stability: Case study at the Niobec Mine, Quebec (Canada). *Geomech. Energy Environ.*, 25, 100194. DOI: 10.1016/j.gete.2020.100194
- Sainsbury, B.L. and Sainsbury, D.P.: 2017, Practical use of the ubiquitous-joint constitutive model for the simulation of anisotropic rock masses. *Rock Mech. Rock Eng.*, 50, 1507–1528. DOI: 10.1007/s00603-017-1177-3
- Singh, B. and Goel, R.K.: 2011, In situ stresses. In: Singh, B. and Goel, R.K. (Eds.): *Engineering Rock Mass Classification*. Butterworth-Heinemann, Oxford, 345–350. DOI: 10.1016/B978-0-12-385878-8.00028-8
- Sjöberg, J., Christiansson, R. and Hudson, J.A.: 2003, ISRM suggested methods for rock stress estimation: Part 2: overcoring methods. *Int. J. Rock Mech. Min. Sci.*, 40, 7–8, 999–1010. DOI: 10.1016/j.ijrmms.2003.07.012
- Souček, K., Vavro, M., Staš, L., Kaláb, Z., Koniček, P., Georgiovská, L., Kaláb, T., Konečný, P., Kolcun, A., Králová, L., Kubina, L., Lednická, M., Malík, J., Martinec, P., Ptáček, J., Vavro, L., Waclawik, P. and Zajíčková, V.: 2018, Complex geological characterization of URF Bukov – part I – Geotechnical characterization. RAWRA Technical Report (No. 221/2018), Czech Radioactive Waste Repository Authority, Prague, 345 pp., (in Czech).
- Souček, K., Vavro, M., Staš, L., Vavro, L., Waclawik, P., Koniček, P., Ptáček, J. and Vondrovic, L.: 2017, Geotechnical characterization of Bukov underground research facility. *Procedia Eng.*, 191, 711–718. DOI: 10.1016/j.proeng.2017.05.236
- Stephansson, O. and Zang, A.: 2012, ISRM suggested methods for rock stress estimation—part 5: establishing a model for the in situ stress at a given site. *Rock Mech. Rock Eng.*, 45, 6, 955–969. DOI: 10.1007/s00603-012-0270-x
- Vavro, M., Souček, K., Staš, L., Waclawik, P., Vavro, L., Koniček, P. and Ptáček, J.: 2015, Application of alternative methods for determination of rock quality designation (RQD) index: a case study from the Rožná I uranium mine, Strážek Moldanubicum, Bohemian Massif, Czech Republic. *Can. Geotech. J.*, 52, 10, 1466–1476. DOI: 10.1139/cgj-2014-0377
- Wang, J., Chen, L., Su, R. and Zhao, X.: 2018, The Beishan underground research laboratory for geological disposal of high-level radioactive waste in China: planning, site selection, site characterization and in situ tests. *J. Rock Mech. Geotech. Eng.*, 10, 3, 411–435. DOI: 10.1016/j.jrmge.2018.03.002
- Zang, A. and Stephansson, O.: 2010, Stress field of the Earth's crust. Springer, Dordrecht, 225–252. DOI: 10.1007/978-1-4020-8444-7
- Zhang, Y. and Mitri, H.S.: 2008, Elastoplastic stability analysis of mine haulage drift in the vicinity of mined stopes. *Int. J. Rock Mech. Min. Sci.*, 45, 4, 574–593. DOI: 10.1016/j.ijrmms.2007.07.020